Math. Model. Nat. Phenom. 17 (2022) 15
https://doi.org/10.1051/mmnp/2022013

Mathematical Modelling of Natural Phenomena
www.mmnp-journal.org

STUDY OF ARCHITECTURAL FORMS OF INVASIVE CARCINOMA BASED ON THE MEASUREMENT OF PATTERN COMPLEXITY

Dmitry Bratsun* and Ivan Krasnyakov

Abstract. Several years ago, a new paradigm of cancer perception emerged, considering a tumor not as a senseless heap of cells but as a self-organizing heterogeneous tissue of cancer cells that collectively fight for survival. It implies that the various architectural forms that a tumor takes during its growth are not occasional but are a synergistic response of a group of cancer cells in competition for the organism's resources. In this work, we generate various patterns of a two-dimensional tumor using our previously developed individual-based model mimicking carcinoma features. Every cell is represented by a polygon dynamically changing its form and size. The dynamics of tissue are governed by the elastic potential energy. We numerically obtain various patterns of carcinoma and estimate empirical spatial entropy and complexity measures applying the approach based on the fast finite shearlet transform. We show how the complexity of growing carcinoma changes over time and depending on the values of the cell intercalation parameters. In each case, we give a rational explanation of why this form is beneficial to the tumor. Our results show that one can use complexity measurements for quantitative classification of tumors obtained *in silico*, which potentially could find its application in medical practice.

Mathematics Subject Classification. 92C17.

Received November 14, 2021. Accepted April 6, 2022.

1. Introduction

Until recently, a cancerous tumor was believed to be a homogeneous accumulation of transformed and degraded cells that have lost their connection with the tissue [26]. Once out of control, cancer cells can quickly divide, due to which the tumor grows, affecting the surrounding healthy tissue. Finally, cancers comprise a large family of diseases that involve abnormal cell growth with the potential to invade or spread to other parts of the body. Although this picture includes evident facts, it cannot explain the incredible vitality of malignant tumors, which makes these diseases extremely dangerous.

Recent studies showed that a tumor is a kind of organ that lives by its rules [15]. Based on this new understanding, in [48], a malignant tumor was even compared to "the village", highlighting the systematic organization of processes within the tumor and the differentiation of cellular elements. It is not to say that researchers did not understand this before. For example, earlier works [13, 36], which studied an artificially introduced intratumoral heterogeneity in mouse models, came to the same conclusion. Heppner [24] stated that cell subpopulations of the same tumor differ in a growth rate, drug response, and ability to metastasize. Some

Keywords and phrases: Tumor structures, collective cell migration, cancer modeling, complexity measurement.

Department of Applied Physics, Perm National Research Polytechnic University, 614990 Perm, Russia.

* Corresponding author: dmitribratsun@rambler.ru

experiments with cloned cancer cells could already be interpreted in the framework of the synergetics paradigm, more than just competition and struggle for resources [13]. However, such studies were largely unnoticed due to the prevalence of the concept of a tumor considered as a structureless group of degenerated cells. Tabassum and Polyak [48] provided an excellent overview of articles that have addressed the heterogeneous nature of cancerous tumors. Authors emphasized that variations in resource availability within a tumor, such as differentiated access to nutrients and oxygen due to tumor architecture, may be the driving force that generates intratumoral heterogeneity.

As an example of experimental works of a new wave, let us mention the studies of carcinoma, which is a malignancy that develops from epithelial cells [11, 12, 17, 28]. For example, Krakhmal *et al.* [28] reported the various breast cancer structures arising even from identical cells. These structures help cancer cells to jointly protect their "village" against different types of therapies, as well as to increase the metastatic capacity [11, 12]. As is was shown, an epithelial-mesenchymal (hereafter EM) transition plays a decisive role in switching carcinomas to the various types of invasion [3, 11, 17, 28]. The EM-transition is a standard process, which takes place whenever a cellular tissue is involved in intensive motion. For example, one could observe the transition during wound healing or morphogenesis of the organs [44]. Details of the molecular mechanism of the way the EM-transition contributes to tumor formation are not yet known. However, one observes that the transition typically accompanies the development of tumors [31]. Finally, when looking for cancer medicine, one should take into account that cancer is a sophisticated self-organized system that can evolve and adapt to changes in the surroundings and modify its behavioral patterns [18, 35].

The literature devoted to the mathematical modeling of cancer has a large number of works [8, 10]. Papers [2, 29] provided more recent reviews of modeling approaches. Although continuous-medium models still represent most of the efforts of theorists, in our opinion, the most promising direction is the construction of individual-based models. This approach is based on the description of the properties of individual elements of a complex system. Here, one considers cells as separate dynamic objects, each with its evolution. Early attempts of discrete modeling were associated with the use of cellular automata [7, 43]. Another modeling technique includes the simulation of individual cell dynamics based on spherical particles or deformable elements [14]. The sphere in this model mimics a cell. The force acting between spheres depends on the distance between their centers. Cells can divide, die, and change their phenotype.

A more recent approach takes into account the geometry of the cell and the possibility of its deformation. The discrete modeling based on individual dynamics of cells provides more detailed information on the behavior of tissue. There are various implementations of the deformable cell model. Viktorinova *et al.* [49] considered the problem of the geometric polarization of cells in tissue. Salm and Pismen [44] studied the problem of wound healing. The phenomenon of cell migration during tumor development was considered in [32]. Bratsun *et al.* [2] proposed a multiscale chemo-mechanical model of cancer tumor development based on the approach developed in [44]. The model accounted for the possibility to transform a normal cell into a cancer one triggered by a local failure of spatial synchronization of the circadian rhythm. Bratsun *et al.* [3] modified the model taking into account that carcinoma is a heterogeneous entity comprising cells of different phenotypes performing different functions in a tumor. The phenotype of each cell was determined by its environment and could dynamically change via an EF transition and vice versa. Numerical simulations showed the different subtypes of invasive carcinoma identified with the histological samples.

Here, it is worthy to notice that tumors are still classified on the basis of histological sections [23, 46]. The oncologist determines the type of tumor by the sample morphology. He estimates the shape of the structure, its microenvironment, the approximate number of cells but relies more on his experience and intuition. Genetic testing also helps the doctor make a decision. Based on the above information, it is impossible to trace the evolution of a tumor from its appearance to the moment of taking a sample. Thus, there is a need for an objective method of tumor classification that would assist the less experienced doctor in making a diagnosis.

Let us discuss briefly on mathematical methods of image processing. One of the most popular methods is the Fourier transform. For example, in a recent paper [47], the Fourier transform was applied to infrared spectroscopy data for the early detection of cancer. Fourier transform infrared spectroscopy certainly can improve clinical decision-making and patient outcomes by detecting biochemical changes at the molecular level. Another

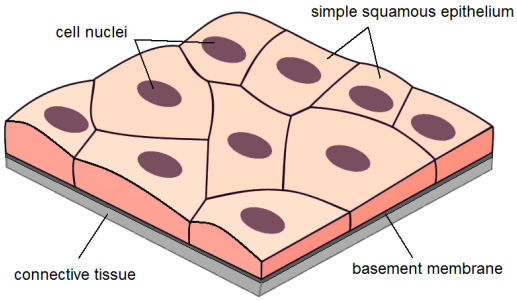

FIGURE 1. Schematic presentation of simple squamous epithelium.

method, wavelet analysis, was also used for the early diagnosis of diseases in works [37, 38]. Its popularity is because it has the inherent advantages of the Fourier transform, and the results can be presented more clearly (in space and frequency). The choice of a specific type of wavelet function depends on the analyzed signal, and here the researcher has to rely on his intuition and experience. Bandt and Pompe [1] were the first who introduce complexity parameters for time series based on comparison of neighboring values. They showed that the introduced permutation entropy is similar to Lyapunov exponents over the wide ranges of parameter values for the well-known family of logistic maps. The advantages of the method were declared to be its simplicity and fast calculation. Rosso *et al.* [42] have successfully applied the ideas of [1] to differentiate chaotic time series from stochastic ones. They have constructed a diagram called an entropy-complexity plane, which was first proposed by López-Ruiz *et al.* [33], by plotting the relative entropic measure versus the permutation entropy. Ribeiro *et al.* [41] used a two-dimensional extension to the permutation entropy suggested in [1] and constructed a method to obtain complexity-entropy pairs for texture images. They successfully demonstrated the operation of the algorithm on Brodatz textures [5]. Later, Zunino and Ribeiro [51] generalized the original algorithm to obtain multiscale and direction-sensitive estimates of entropy and complexity. Biomedical applications of the permutation entropy were discussed in [50]. Finally, Brazhe [4] suggested new spatial entropy and complexity measures for two-dimensional patterns. The approach was based on the disequilibrium concept and was built on statistics of directional multiscale coefficients of the fast finite shearlet transform. Shannon entropy and Jensen-Shannon divergence measures were employed. The algorithm was validated in numerical experiments with a gradually decaying periodic pattern and Ising surfaces near-critical state.

In this work, we numerically generate various architectural forms of carcinoma using the individual-based model we developed earlier. The tumors are represented by a series of two-dimensional images enabling us to evaluate spatial entropy and complexity of patterns based on the fast finite shearlet transform. We show that each type of carcinoma has a unique spectrum on an entropy-complexity plane. Thus, the subjective perception of the pattern can be tested by objectively measuring its informational characteristics. The paper is organized as follows: in Section 2, we shortly describe the mathematical model we apply to mimic the development of carcinomas. The algorithm to calculate spatial entropy and complexity measures is discussed in Section 3. Section 4 presents the numerical results. In Section 5, we discuss the obtained results and make the conclusions.

2. Individual-based model of invasive carcinoma

2.1. Epithelial tissue

In this work, we consider the processes occurring in the epithelial tissue. The epithelium is a collection of differentiated cells closely adjacent to each other in the form of a layer resting on the basement membrane (Fig. 1). Desmosomes that connect cells are multiple submicroscopic flagella on the adjacent surfaces of neighboring cells. Epithelial tissues in the body always occupy a borderline position. For example, the epithelium covers the surface of the skin, the cornea of the eye, serous membranes, the inner surface of the hollow organs of

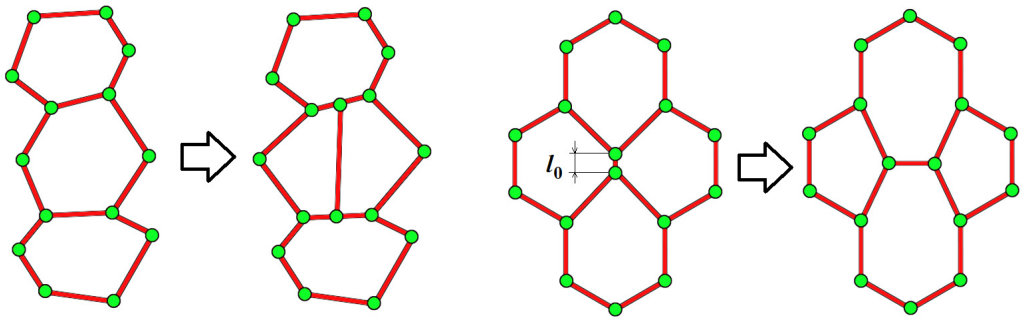

FIGURE 2. Elements of chemomechanical model of carcinoma developing in a simple squamous epithelium with individual dynamics of cell: (a) cell division; (b) cell intercalation.

the digestive, respiratory and genitourinary systems, and also forms glands. On the one hand, the epithelium is a convenient medium for modeling since some of its varieties (for example, simple squamous epithelium shown in Fig. 1) is a quasi-two-dimensional cellular medium. On the other hand, the epithelium performs the most vital functions of protecting the body from the external environment.

2.2. Discrete epithelium model with individual cell dynamics

A discrete model of the epithelium, which allows us to follow the dynamics of individual cells and describe the behavior of the tissue as a whole, was first proposed in work by Salm and Pismen [44]. Some properties of this model then were refined/simplified in [2, 3, 29]. Let us briefly describe the main properties of the model. The cell is imitated by a polygon. The number of sides of a polygon is an individual feature of each cell and can dynamically change in time. To eliminate the appearance of topological defects in the lattice, the angle at the vertex of any polygon cannot exceed 180 degrees. In real tissue, this condition is usually not violated for cells of the epithelial phenotype (hereafter E-cells). However, mesenchymal cells (M-cells), due to their cytoskeleton, can acquire more diverse forms. We believe that cells everywhere are tightly adjacent to each other, forming a continuous surface without gaps, just as it happens in the natural epithelium (Fig. 1).

In the model, potential energy determines the evolution of tissue

$$E = \frac{1}{2}\sum_i \left[\mu L_i^2 + \eta(A_i - A_0)^2\right], \tag{2.1}$$

where L_i is the perimeter of an ith cell, A_i is its area, and the summation is over all cells in the layer. The first term in (2.1) describes the action of forces tending to reduce the perimeter of each cell, and the second one represents the cell's resistance to stretching and compression forces, as a cell attempts to preserve its average area A_0. The elasticity coefficients of the medium μ and η are the control parameters of the model determining the deformation properties of the medium.

Epithelial tissue evolves by moving the vertices of the polygons. The mechanical force acting on the jth node (the nodes of the polygon are indicated in Fig. 2 by green circles) is determined in the standard way:

$$\mathbf{F}_j = -\frac{\partial E}{\partial \mathbf{R}_j} \tag{2.2}$$

where $\mathbf{R}_j$ is the radius vector of the jth node. The displacement of the vertices means the deformation of the cell. It results in a change in the cell's area and perimeter.

Let us discuss the equation of motion for cells. In a healthy epithelium, cells are included in one layer, are connected with neighboring cells by desmosomes, and cannot move through the tissue. In this case, the tissue is a classical deformable rigid body. However, such a medium can undergo sudden liquefaction if the tissue instructs the cells to move. For example, this situation occurs when tissue is injured [44]. Another case arises in the case of a tumor. Cancer cells can migrate both in large groups and individually [3]. Such movement meets significant resistance since the permeability of this medium is very low. Thus, we conclude that the most appropriate apparatus for describing the motion of cells in tissue is Aristotle's mechanics, not Newton's:

$$\mathbf{V}_i = \frac{\mathrm{d}\mathbf{R}_i}{\mathrm{d}t} = K\mathbf{F}_i\Theta(\mid \mathbf{F}_i \mid -F_0), \tag{2.3}$$

where K is the mobility coefficient, Θ is the Heaviside step function, and F_0 is a parameter that determines the critical value of force, below which the node remains motionless if $|\mathbf{F}_i| < F_0$. The latter ensures that any local motion in the medium begins if the external force exceeds a certain threshold. This condition is necessary to impart general stability and a certain inertness to the tissue.

As is known, tissue grows due to cell division. We assume that the probability p of cell division depends on the number of its nodes:

$$p_{\mathrm{div}} = p_0 q^{n-6} \tag{2.4}$$

where p_0 and q are the parameters. In the case $q > 1$, the division of cells with a large number of nodes is preferable, although the hexagon remains the most advantageous cell form. The process of cell division occurs as shown in Figure 2(a). Immediately after the emergence of a new cell, the program registers it, and the cell begins its individual evolution in the epithelial tissue. At the same time, a new cell inherits from the mother cell the instantaneous values of chemical and mechanical fields at the time of division. Thus, the algorithm mimics mitotic cell division.

The process of intercalation of cells works as a tool for weakening local stresses in the tissue in the event of its significant structural rearrangement [16, 19]. The simplest intercalation algorithm can be written as follows:

$$p_{\mathrm{int}} = \begin{cases} 1 & , \quad l_i < l_0 \\ 0 & , \quad l_i \geq l_0 \end{cases} . \tag{2.5}$$

Algorithm (2.5) is triggered if the bridge between the cells becomes less than the critical value l_0 (see Fig. 2(b)). The value l_0 is chosen in such a way that intercalation of healthy cells is rare. In general, the mechanisms of proliferation (2.4) and intercalation (2.5) allow a cell to dynamically change its shape and size by changing the number of vertices of the polygon and their mutual displacement under the influence of external forces.

2.3. Heterogeneous carcinoma model

The development of carcinoma in the epithelium means the appearance of at least one more type of cell in the tissue. To define a new cell species, we introduce a discrete function Z taking only two values: $Z = 0$ for a healthy cell and $Z = 1$ for a cancer cell. This value marks all cells and helps to establish two separate sets of parameter values, which determine the dynamics of normal and cancer tissues.

We consider a tumor as a heterogeneous community of cancer cells with different properties. Following our previous paper [3] we introduce the EM transition index S_i for the ith cancer cell in the following way:

$$S_i = 1 - \frac{1}{N_{0i}} \sum_{j \in adj(i)} Z_j, \tag{2.6}$$

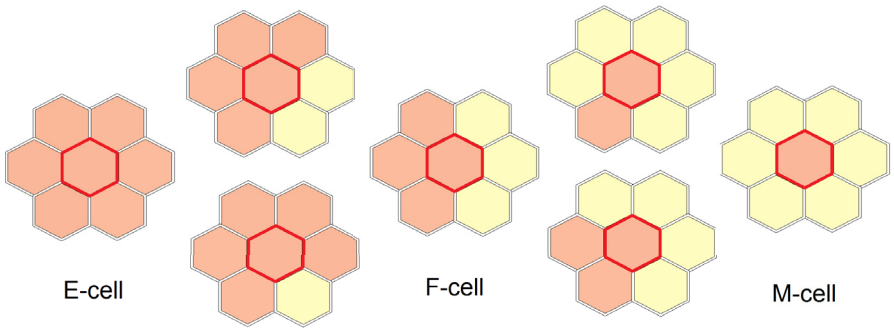

FIGURE 3. The classification of cancer cells in a heterogeneous tumor is determined by the stage of the EM-transition. The cell's phenotype is changing from the left to the right, depending on the value of the index S of the EM transition. The epithelial phenotype (E-cell) is determined when all cells adjacent to the reference cell are cancerous ($S = 0$). The mesenchymal phenotype (M-cell) is implemented at $S = 1$ when all closest neighbors are healthy cells. Frontal cell (F-cell) represents an intermediate phenotype. Cancer and healthy cells are red and yellow, respectively. The reference cell is indicated by the red line.

where N_0 is the total number of the cells adjacent to the ith cancer cell equal to the number of the sides of the corresponding polygon. Summation in equation (2.6) is done overall adjacent cells. So, the variable S defines the phenotype of a cancer cell. The value $S = 0$ corresponds to the epithelial phenotype, while the value $S = 1$, to the mesenchymal phenotype. The intermediate values between 0 and 1 correspond to a mixed EM phenotype, in which we distinguish frontal cells in a separate class (Fig. 3). The above classification is confirmed by experimental observations [17, 28]. One observes differences in the expression of genes and the morphology between F-cells forming the leading edge of a tumor and internal cells located behind. The cells located at a leading-edge often resemble theirs shape and behavior of M-cells and are characterized by a less pronounced ordering and structural organization. The following cells tend to form more tightly packed structures with intensive intercellular contacts (E-cells). In the experiments, the cell's phenotype can be identified by measuring the expression level of cadherin or integrin genes [31], which helps to define the EM transition index. In a real cell, the transition is determined by a set of transcription/translation processes running under the impact of external factors. A cell regenerates by changing its phenotype and then behaves accordingly in the epithelium tissues.

Thus, in our model, the behavior of a cancer cell not only differs significantly from the behavior of healthy E-cells but is also determined by the position it occupies in the cellular society of the tumor. In [3], we developed a system of phenomenological equations based on the Hill function. The probability distribution for the proliferation of each cancer cell depends on its phenotype:

$$p_{\mathrm{div}}^{i} = p_0 q^{n-6} + p_1 \frac{S_i^n \left(1 - S_i\right)^m}{\left(1 + S_i^n\right)\left(1 + (1 - S_i)^m\right)}. \tag{2.7}$$

Here, n and m stand for the parameters of the Hill function, $P_1 = P_1(n, m)$ is the normalization factor depending on n and m. The mobility of cancer cells is governed by the intercalation parameter l_0^{can}. For simplicity, in this work, we will consider this parameter the same for all cancer cells.

2.4. Numerical method to generate a tumor pattern

The system of ordinary differential equations and the related formulas (2.1)–(2.7) describing the dynamics of a heterogeneous carcinoma has been numerically solved by the Euler explicit method, whose stability was

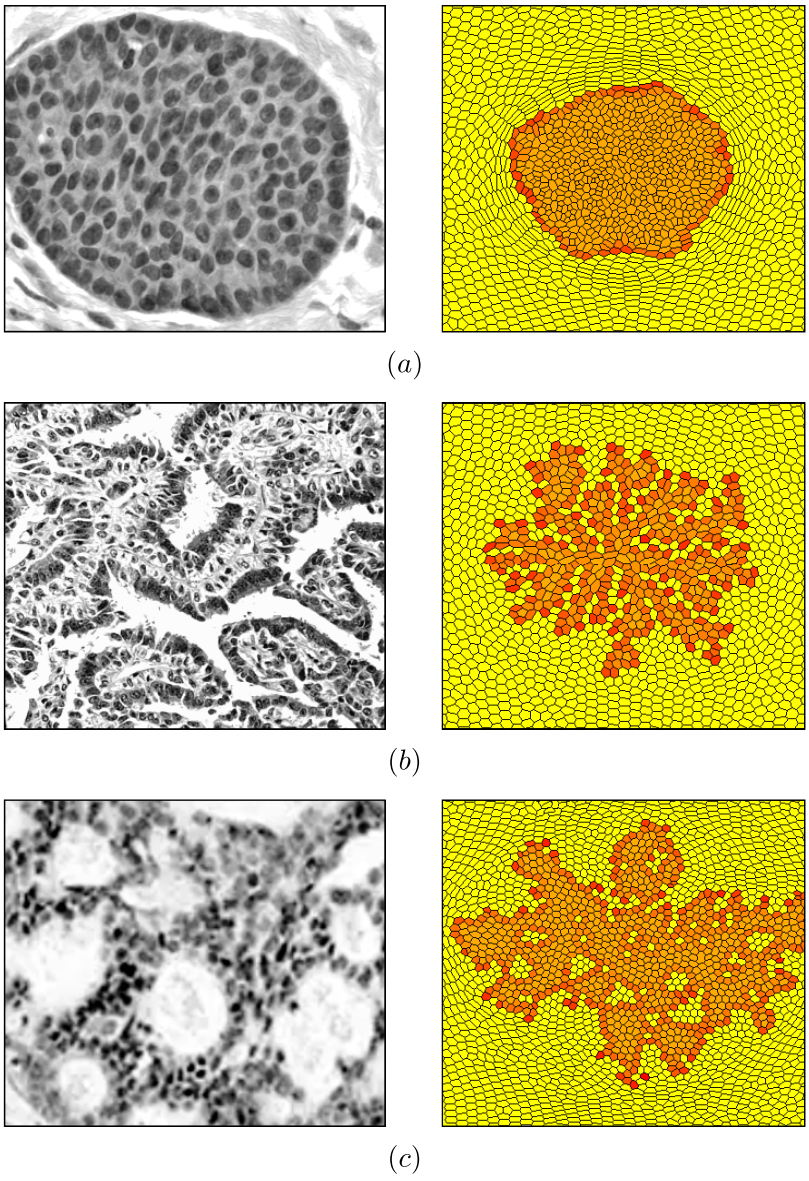

FIGURE 4. Typical carcinoma tumors observed in the histological sections (left) compared to the structures obtained numerically (right) with different values of intercalation parameters [3]: (a) solid tumor at $l_0 = 0.1$, $l_0^{\text{can}} = 0.1$; (b) papillary tumor at $l_0 = 0.4$, $l_0^{\text{can}} = 0.1$; (c) cribriform tumor at $l_0 = 0.1$, $l_0^{\text{can}} = 0.4$.

warranted by a sufficiently short time step $\Delta t = 0.005$. The initial computational domain filled by cells was a stripe bounded by $-30 \leqslant x \leqslant 30$ and $-30 \leqslant y \leqslant 30$. For simplicity, the periodic boundary conditions have been set along the y-axis. Along the x-axis, the cellular structure could evolve freely. The initial configuration of the cellular tissue was always a regular hexagonal lattice comprising about 1500 normal cells. Table 1 gives the values of model parameters, respectively, for normal and cancer cells used in all numerical simulations. Most of the parameter values of the mechanical submodel were calibrated in [2, 3, 44].

TABLE 1. Parameters of the model to simulate the mechanics of normal epithelium and tumor.

species	μ	η	K	F_0	A_0	α	p_0	q
normal cell	1.0	4.5	2.1	0.1	$3\sqrt{3}/2$	0.005	0.0002	1.4
cancer cell	1.0	4.5	2.1	0.1	$6\sqrt{3}/5$	0.005	0.0001	1.4

In this work, we generate tumor patterns formed due to the competition between two species of cells with different elastic properties determined by l_0 (the normal cells) and l_0^{can} (the cancer cells). In fact, these parameters determine the mobility (fluidity) of the medium: the higher its value, the more often the cells intercalate with their neighbors. We consider them as governing parameters of the problem.

Before advancing, we should make the following reservation. By obtaining a variety of carcinoma patterns in numerical simulations, we rely on visual perception of structure when trying to identify it with the WHO nomenclature listed in [46]. Therefore, we can identify the pattern only tentatively. The tumor type is best identified from a list of specific, well-differentiated breast cancers. Thus, in what follows, the terms "papillary" and "cribriform" refer to "papillary-like" and "cribriform-like", respectively.

Figure 4 shows typical structures that are obtained numerically by varying the parameters of intercalation l_0 and l_0^{can}. Figure 4(a) corresponds to the case when the tumor and the surrounding healthy tissue have the same mobility: $l_0 = l_0^{\text{can}}$. We identify this tumor as a solid carcinoma. According to histological observations [3, 28, 34], a solid pattern of carcinoma includes compact continuous lumps of different sizes and shapes consisting either of tiny cells with monomorphic nuclei or of large cells with polymorphic nuclei. Figure 4(b) shows the pattern, which develops at $l_0 = 4l_0^{\text{can}}$. We identify this structure as papillary carcinoma. The primary difference between papillary structure and other carcinomas is that the cancer cells are included in finger-like projections. Under a microscope, the cells appear fern-like [3, 34]. If $l_0 = 0.25l_0^{\text{can}}$, we obtain the tumor identified as a cribriform carcinoma (Fig. 4(c)). The cribriform pattern contains similar nest-like formations. Within the tumor, there are distinctive holes between cancer cells, making it look like Swiss cheese [3, 34].

3. SHEARLET TRANSFORM

Shearlets are a relatively new class of multiscale representation systems, which allows efficient encoding of anisotropic features in multivariate data [20, 30]. Shearlets are a natural extension of wavelets able to overcome wavelet inability of capturing anisotropic features. As is known, wavelets provide an optimal approximation for one-dimensional piecewise continuous functions. They are based on isotropic scaling, which makes them isotropic transforms and, therefore, not suitable for detecting non-isotropic objects. So, wavelets do not perform as well in dimensions larger than one. Figure 5 schematically shows that, unlike the wavelet, which is provided only by the dilation and translation operations, the shearlet is generated by an additional operation, the shearing. Also, since the shearlet transform defines the scaling function using parabolic scaling, it can detect curvilinear structures, as shown in Figure 5. These properties of shearlets provide a more efficient approximation of spatially distributed inhomogeneities. Therefore, shearlets can be seen as the efficient tool for the detection of directional sensitive visual features like edges, corners, textures, and, more generally, patterns occurring in two-dimensional imaging data.

As mentioned above, a shearlet is generated by operations based on the dilation, shearing, and translation of a function ψ, sometimes called the *mother shearlet*, as it follows:

$$\psi_{a,s,t}(x) = a^{-3/4}\psi(A_a^{-1}S_s^{-1}(x-t)), \tag{3.1}$$

where $t \in \mathbb{R}^2$ stands for a translation. In (3.1), the matrices A_a and S_s given by

$$A_a = \begin{pmatrix} a & 0 \\ 0 & \sqrt{a} \end{pmatrix}, \qquad S_s = \begin{pmatrix} 1 & s \\ 0 & 1 \end{pmatrix}, \tag{3.2}$$

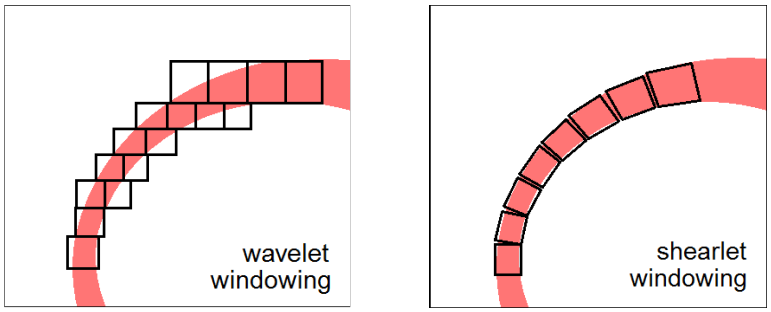

(a) (b)

FIGURE 5. Comparison of wavelet and shearlet-based representations of spatial inhomogeneity in the form of a curved strip: (a) wavelet approximation of the strip by isotropic elements generated by the dilation and translation; (b) shearlet coverage by anisotropic elements denerated by the dilation, translation, and shearing.

define the dilation and shearing, respectively. Here, $a \in \mathbb{R}^+$, $s \in \mathbb{R}$.

As is shown in [20, 30], one can factorize the shearlet ψ in Fourier domain in the following way:

$$\hat{\psi}_{a,s,t}(\omega_1, \omega_2) = \hat{\psi}_1(\omega_1)\hat{\psi}_2\left(\frac{\omega_2}{\omega_1}\right), \tag{3.3}$$

where $\hat{\psi}$ stands for the Fourier transform of ψ. Here, $\hat{\psi}_1$ is a one-dimensional wavelet, and $\hat{\psi}_2$ is any non-zero square-integrable function. By taking into account (3.3), equation (3.1) in Fourier domain becomes

$$\hat{\psi}_{a,s,t}(\omega_1, \omega_2) = a^{3/4}\hat{\psi}_1(a\omega_1)\hat{\psi}_2\left(\frac{\omega_2 - s\omega_1}{\sqrt{a}\omega_1}\right) e^{-2\pi i\omega t}, \tag{3.4}$$

where $\omega = (\omega_1, \omega_2) \in \mathbb{R}^2$ and $\omega_1 \neq 0$.

One of the popular choices for the appropriate functions $\hat{\psi}_1$ and $\hat{\psi}_2$ discussed in [22] is as follows:

$$\hat{\psi}_1(\omega) = \sqrt{\xi^2(2\omega) + \xi^2(\omega)}, \quad \hat{\psi}_2(\omega) = \begin{cases} \sqrt{\zeta(1+\omega)} & \text{for } \omega \leqslant 0 \\ \sqrt{\zeta(1-\omega)} & \text{for } \omega > 0 \end{cases}, \tag{3.5}$$

where

$$\xi(x) = \begin{cases} \sin\left(\frac{\pi}{2}\zeta(|x|-1)\right) & \text{for } 1 \leqslant |x| \leqslant 2 \\ \cos\left(\frac{\pi}{2}\zeta(\frac{1}{2}|x|-1)\right) & \text{for } 2 < |x| \leqslant 4 \\ 0 & \text{otherwise} \end{cases}, \quad \zeta(x) = \begin{cases} 0 & \text{for } x < 0 \\ 35x^4 - 84x^5 + 70x^6 - 20x^7 & \text{for } 0 \leqslant x \leqslant 1 \\ 1 & \text{for } x > 1 \end{cases}. \tag{3.6}$$

Figure 6 presents the density plot of the series of dilated and sheared mother shearlet defined by (3.4)–(3.6) in the time domain. The graphs of shearlet functions are shown for three successively increasing scales and a series of orientations controlled by vertical and horizontal shift operations. Thus, used as a spatial filter, the scaled and sheared copies of ψ can emphasize prevalent anisotropic features at different spatial scales and orientations.

We further define the continuous shearlet transform $SH(f)$ of a signal $f \in \mathbb{R}^2$ as

$$SH(f)(a, s, t) \equiv < f\psi_{a,s,t} >= a^{3/4} \int \hat{f}(\omega_1, \omega_2)\hat{\psi}_1(a\omega_1)\hat{\psi}_2\left(\frac{\omega_2 - s\omega_1}{\sqrt{a}\omega_1}\right) e^{-2\pi i\omega t} d\omega_1 d\omega_2. \tag{3.7}$$

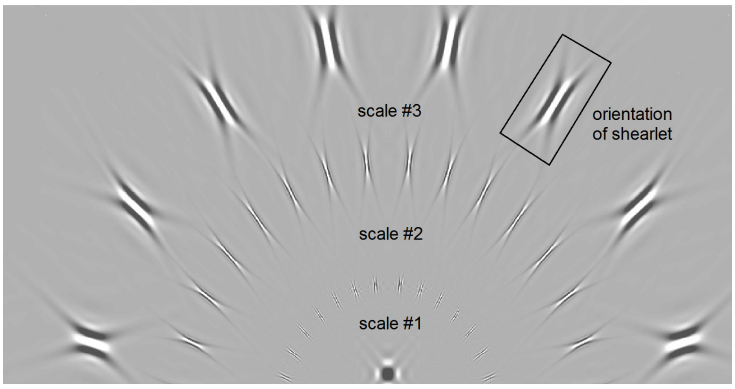

FIGURE 6. Set of shearlet basis functions in the time domain showing mother shearlet $\psi_{a,s,t}$ of three different scales and different orientations governed by the horizontal and vertical shears.

We can consider the data given by a digital image as a two-dimensional signal $f(x, y)$. Therefore the shearlet transform (3.7) is the convolution of the image with scaled, sheared, and shifted copies of a mother shearlet function $\psi_{a,s,t}$. As a result, we obtain an efficient tool to account for different scales and orientations of features contained in the image.

To discretize the shearlet transform (3.7), we apply a fast finite discrete shearlet transform (FFST), an approach initially developed in references [21, 22]. We consider the FFST of a square digital image $f \in \mathbb{R}^{N,N}$ as a function sampled on the grid $\{m1/N, m2/N\}$, $m_1, m_2 = 0, \ldots, N-1$. Then the parameters of scaling a, shear s, and translation t are discretized as

$$a_j = 2^{-2j}, \quad j = 0, \ldots, j_0 - 1, \qquad s_{j,k} = k2^{-j}, \quad -2^j \leqslant k \leqslant 2^j, \qquad t_m = \left(\frac{m_1}{N}, \frac{m_2}{N}\right), \tag{3.8}$$

respectively. In (3.8), $j_0 = \log_2 \sqrt{N}$ stands for the number of considered scales.

Finally, the discrete shearlet transform is defined as a mapping from image f to a set of shearlet coefficients $\psi_{j,k,m}$:

$$SH(f)(a_j, s_{j,k}, t_m) \equiv < f\psi_{j,k,m} >= 2^{-\frac{3}{2}j} \sum_{\omega} \hat{f}(\omega_1, \omega_2)\hat{\psi}_1(2^{-2j}\omega_1)\hat{\psi}_2\left(2^j \frac{\omega_2}{\omega_1} - k\right) e^{-2\pi i \frac{\omega_1 m_1 + \omega_2 m_2}{N}}. \tag{3.9}$$

As it is noted in [4], the translation operation is redundant in the problem under the consideration. It means that we can simplify the representation of the shearlet coefficients $\psi_{j,k,m}$ to

$$\hat{\phi}_{j,k} = \hat{\psi}_{j,k,m}|_{m=0}. \tag{3.10}$$

The assumption (3.10) enables us reducing the result of the FFST to a set of matrices $\Omega_{j,k}$ including only dilation and shearing operations:

$$SH(f) =< f\phi_{j,k} >= \{\Omega_{j,k}(x, y)\} \equiv \{\Omega_i(x, y)\}, \tag{3.11}$$

where we introduce consecutive indexing i to run though all scales a_j and shears $s_{j,k}$ (see Fig. 6).

The discrete shearlet transform can be efficiently computed by applying the 2D fast Fourier transform and its inverse [22]. For an image of size $N \times N$, the computational complexity of the FFST is found to be $O(N^2 \log N)$.

4. Shearlet-based complexity and spectral entropy measures

As noted above, the doctor classifies the type of tumor based on the subjective perception of the histological section. Likewise, we identified the cancerous structures obtained numerically based on the subjective perception of the pattern. In both cases, such an approach must be supported by some objective measurements. Several years ago, Crutchfield [9] reasonably noted that there was still no universal approaches to a comparative assessment of the complexity of different spatial patterns emerging in the processes of self-organization and morphogenesis. However, some attempts to solve this problem have recently appeared in the literature. In this work, we evaluate the relative complexity of the emerging structures of tumors represented by two-dimensional images using the methods proposed in papers [1, 4, 33, 41, 42].

The first measure is the normalized entropy $H[P]$, which is obtained by applying Shannon's entropy $S[P]$ to some probability distribution P:

$$H[P] = \frac{S[P]}{S_{\max}}, \tag{4.1}$$

where $S[P] = -\sum P \log P$. The value of $S_{\max}$ is obtained by considering all the accessible states to be equiprobable. We expect that the entropy $H[P]$ will indicate some correlation in the distribution. Entropy is one of the most powerful metrics of a signal. It is associated with disorder degree (randomness) and unpredictability. By definition, the value $H[P] = 1$ corresponds to a completely random state, while the value $H[P] = 0$ corresponds to the state of a perfect crystal.

There are several ways to construct the probability distribution P for 2D image analysis. For example, Ribeiro *et al.* [41] employed the permutation entropy. Brazhe [4] proposed an alternative approach based on the definition of spectral entropy first introduced in [39]. The author was able to use shearlets to provide for a two-dimensional extension of this measure. The new approach loses slightly to the algorithm suggested in [41] in terms of the implementation simplicity and speed of calculation, but, what is important, it introduces local spectral entropy. For our problem, the local formulation of entropy is more appropriate since the tumor gradually grows. Another difficulty of our problem is that we need to identify the significant complexity of the pattern composed of discrete cells against the background of the cellular lattice. Also, the epithelium significantly deforms when evolving. Therefore its complexity must be subtracted from the complexity of the system as a whole.

So, following the approach proposed in [4], we study two-dimensional patterns given by the image $f(x, y)$ and introduce the global probability distribution $P = \{P_i, i = 1, \ldots, N\}$ computed for all pixels of the image:

$$P_i = \frac{\sum\limits_{x,y} E_i(x, y)}{\sum\limits_{j,k,x,y} E_{j,k}(x, y)}, \tag{4.2}$$

where the energy of shearlet coefficients Ω_i defined as

$$E_i(x, y) = \Omega_i^2(x, y) \tag{4.3}$$

describes how the corresponding scales and orientations are represented at a given location of the image $f(x, y)$.

The local version of probability distribution $P_i^{local}(x, y)$ is defined as

$$P_i^{(local)}(x, y) = \frac{E_i^*(x, y)}{\sum\limits_{j,k} E_{j,k}^*(x, y)}, \tag{4.4}$$

where $E_i^*(x,y)$ stand for shearlet power coefficients, which are locally averaged with a Gaussian smoothing kernel of standard deviation σ:

$$E_i^*(x,y) = \sum_{X,Y} \frac{1}{2\pi\sigma^2} e^{-\frac{X^2+Y^2}{2\sigma^2}} E_i(x-X, y-Y). \tag{4.5}$$

In contrast to (4.2), the local formulation of the probability distribution (4.4) is very important for this study, since a cancer tumor is an evolving structure that emerges and gradually grows in a certain region of space. In the course of this evolution, we should be able to follow the processes in the area, where the tumor develops, and distinguish them from the processes taking place elsewhere.

At this stage, we can clarify (4.1) in the following way:

$$H[P] = -\frac{\sum\limits_{i=1}^{N} P_i \log_2 P_i}{\log_2 N}, \tag{4.6}$$

where $S[P_e] = \log_2 N$ is calculated for the equiprobable distribution P_e, where all shearlet features are equally represented by $P_i = 1/N$.

The other measure [42] is defined by

$$C[P] = Q[P, P_e] H[P], \tag{4.7}$$

where $Q[P, P_e]$ stands for the normalized Jensen-Shannon divergence, which describes a distance between an observed and the equiprobable distributions. The advantage of the complexity measure (4.7) is that it quantifies both randomness and degree of spatial correlations in the data. It is declared that this measure allows revealing the intrinsic complexity resulting from the system properties, in contrast to the extrinsic complexity, appearing, for example, due to remainders of an ordered state melted by noise.

In terms of the probability distribution (4.2), we can rewrite (4.7) in the following way:

$$C[P] = \frac{H[P]}{J_{\max}} \left(S\left[\frac{P+P_e}{2}\right] - \frac{1}{2}(S[P] + S[P_e]) \right), \tag{4.8}$$

where

$$J_{\max} = -\frac{1}{2} \log_2 \frac{(N+1)^{1+\frac{1}{N}}}{4N}.$$

After calculating the spectral entropy (2.7) and complexity (4.7) measures of the pattern, the basic information about the properties of the system under consideration can be obtained from its plotting on the complexity-entropy plane [4, 33, 42]. One asymptotic case includes an ordered spatially periodic structure with a single temporal or spatial scale, which has a low value of entropy but also a low level of complexity ($H \ll 1$, $C \ll 1$). In the case of the prevalence of noise, which suppresses any signal, one observes a lack of ordered structures, and the entropy is maximal, while complexity is still low ($H \approx 1$, $C \ll 1$). The most intriguing cases lie between these two extreme situations. They represent patterns with nontrivial regularities and correlations.

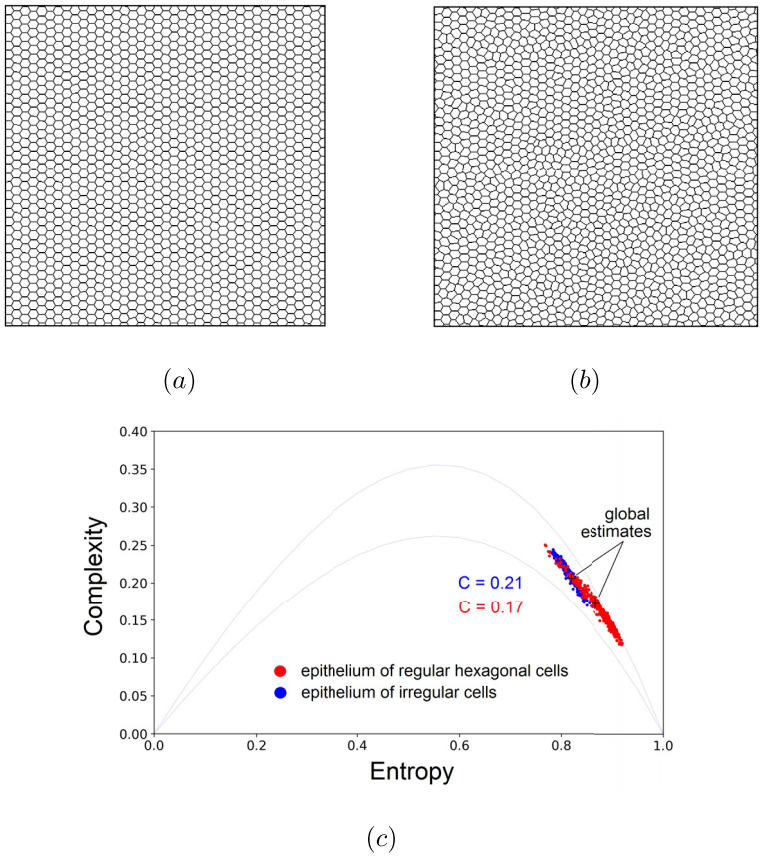

FIGURE 7. Cellular structure generated by the program for the case of an epithelium composed of regular hexagonal cells (a), irregular cells (b). An irregular pattern is generated by the evolution of a hexagonal structure, with the condition of cell division at each time step with a probability of 0.02. (c) Entropy and complexity spectra taken from local values and shown on the H–C plane for the input images (a) and (b). Global estimates for each pattern are indicated by crosses, complexity values are shown explicitly in the figure.

5. NUMERICAL RESULTS

5.1. Complexity of a cellular pattern of the epithelium

Before considering cancerous structures, let us discuss the spectral entropy and the complexity measures applied to the cellular structure of the epithelium. We should bear in mind that epithelial tissue is discrete, in which the cell is the minimum element (pixel). On the one hand, this fact simplifies the analysis since the cell sets the natural scale for any structure that appears in the tissue. On the other hand, any cellular medium itself exhibits a certain regularity that we must evaluate in terms of the entropy and complexity measurements.

To test the cellular environment of the epithelium, we prepared two samples. The first sample shown in Figure 7(a) is a plane composed of identical regular hexagonal cells. As is known, there are only three types of regular tessellations of the flat: triangular, square, and hexagonal [6]. The most natural tessellation is a plain one made of regular hexagons. In geometry, the hexagonal tessellation is an ordered tiling of the Euclidean plane, in which three hexagons meet at each vertex. This form of filling the plane is widespread in nature (honeycomb, Rayleigh-Bénard convective cells, thermocapillary convection, graphene, and so on). Besides, the hexagon is the energetically preferred shape for the cell since this shape is closest to a circle. In fact, the epithelium rarely has

such an ordered structure as a hexagonal pattern. Therefore, we prepared another epithelium sample shown in Figure 7(b). This cellular structure looks much less regular and consists of irregular polygons with different numbers of vertices. We obtained this structure by integrating over 20 units of time the equations of epithelial mechanics (2.1)–(2.7) starting with a hexagonal tessellation. We set an evolutionary condition under which, at each time step, cells divide with a probability of 0.02. Thus, the initially perfectly regular cellular pattern quickly became irregular, although it is also not random.

Figure 7(c) shows the local spectra of entropy and complexity of the above-described cellular structures plotted on the H–C plane. The global values of entropy and complexity are also shown in the figure. As one can see from the figure, a regular hexagonal lattice has characterized by the entropy $H_{\text{hex}} = 0.87$ and the complexity $C_{\text{hex}} = 0.17$, while an irregular lattice has the same measures equal to $H_{\text{irreg}} = 0.81$ and $C_{\text{irreg}} = 0.21$, respectively. We can see that the algorithm gives a lower entropy value for the structure in Figure 7(b) since it looks less like a crystal lattice than a hexagonal pattern. In contrast, the measurement of global complexity gives an irregular pattern a larger value. In this case, intuition finds it difficult to give a correct interpretation since the complexity defined by (4.7) is a balance between the level of entropy and the instability that generates the pattern [4]. Therefore, a numerical estimate of C is a valuable quantitative measure that leads to the conclusion that the global complexity of an irregular pattern is slightly greater than that of a regular hexagonal pattern: $C_{\text{irreg}} > C_{\text{hex}}$. Complexity spectra taken from local values and presented in Figure 7(c) also confirm this conclusion.

5.2. Complexity of a growing carcinoma

Let us consider the temporal dynamics of two types of carcinomas, papillary and cribriform tumors. In each case, the initial configuration includes an epithelium composed of irregular polygons similar to that shown in Figure 7(b). A species of cancer cells initially consists of only one cell in the center of the computational domain. The integration of the equations is completed at time $t = 150$. Figure 8(a) shows the time evolution of the epithelium, in which cancer and healthy cells are marked in red (corresponds to the value of the state function $Z = 1$) and in yellow ($Z = 0$), respectively. In each case, the development of the tumor is shown for consecutive times $t = 0, 30, 60, 90, 120, 150$. When evaluating cancerous structures at the final moment $t = 150$ based on subjective perception, one has difficulty making an unambiguous conclusion about which pattern is more complex. Both tumors look quite intricate and have a spatial order determined by instability (compare the upper and lower frames at Fig. 8(a), $t = 150$). One can notice that the cribriform structure contains more cancer cells. Generally, the tumor in our model grows thanks to inner cells (E-cells and F-cells), which divide much more intensively than M-cells (see formula (2.7)). It is not difficult to understand why this is so: the more mobile the cell (means higher the value S of its EM-transition index), the less this cell is prone to division. The structure of a papillary tumor is such that cells of the mesenchymal phenotype ($S > 0.5$) prevail there, while for a cribriform tumor, the opposite is true ($S < 0.5$).

To get a quantitative estimate of the complexity of the pattern, we applied it to the frames shown in Figure 8(a) the computational algorithm described above. We prepared images as follows: each frame of evolution was cropped in such a way as to contain only a cellular space of the same size, and the color picture then was converted into a grayscale palette. Figure 8(b) shows the variation in the global complexity value C for both types of carcinoma over time. One can notice that the appearance of a tumor results in a decrease in the value of C. The complexity of the image at the initial stage of tumor growth is defined by the complexity of the background cellular structure. Therefore, this effect is associated with increasing deformations of healthy cells that surround the tumor. The algorithm considers these deformations as noise, which leads to an increase in the spectral entropy of the pattern. It is why we do not consider a solid tumor in this work, as it has less structural complexity. Moreover, a solid carcinoma turned out to be an entropy generator, judging by the comparison of its entropy with that of normal cellular tissue.

With the growth of the cancer cluster, the complexity value gradually begins to increase for both papillary and cribriform tumors (Fig. 8(b), $t > 40$). This effect occurs exclusively due to the processes of self-organization in the community of cancer cells. Figure 8(c), which demonstrates the local complexity fields, convincingly proves

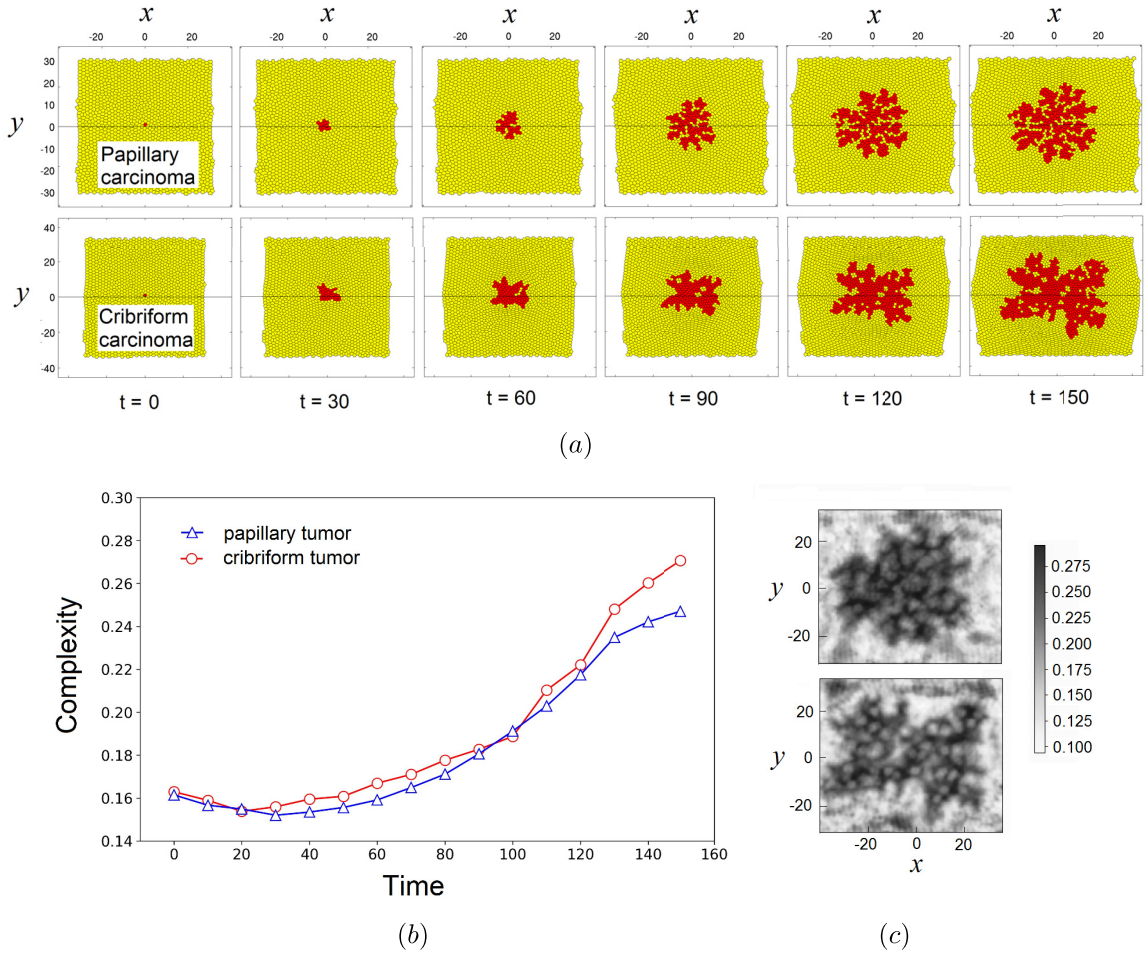

FIGURE 8. (a) Examples of simulated carcinoma patterns at successive times. The intercalation parameters for a papillar tumor are fixed to $l_0 = 0.4$, $l_0^{\text{can}} = 0.1$. The intercalation parameters for a cribriform tumor are fixed to $l_0 = 0.1$, $l_0^{\text{can}} = 0.4$; (b) Global complexity estimates calculated for carcinoma patterns shown at successive times $t = 0, 30, 60, 90, 120, 150$; (c) Local complexity fields shown for the papillar (*up*) and cribriform (*bottom*) tumors at $t = 150$.

it. The synergistic order arises and grows due to the tumor, not due to the surrounding tissue. It is interesting to notice that, at the very beginning of evolution, one faces a problem choosing between papillary and cribriform tumors since the difference between them is comparable to the calculation error. However, with the growth of each of the tumors, it becomes clear that cribriform carcinoma is more complicated (Fig. 8(b), $t > 120$). The difference between them looks negligible, however, clearly recorded in dozens of numerical experiments: the complexity of a cribriform tumor is about $C_{\text{cri}} \approx 0.27$ versus $C_{\text{pap}} \approx 0.25$ for a papillary one at time $t = 150$). Figure 8(c) explains why this is the case. One can see that the algorithm gropes for the characteristic size of the cribriform pattern (spots in the tumor). The same effect is less pronounced in the papillary pattern.

5.3. Parametric study

In this section, we discuss the tumor structure changes if two control parameters of the problem, l_0 and l_0^{can}, are varied.

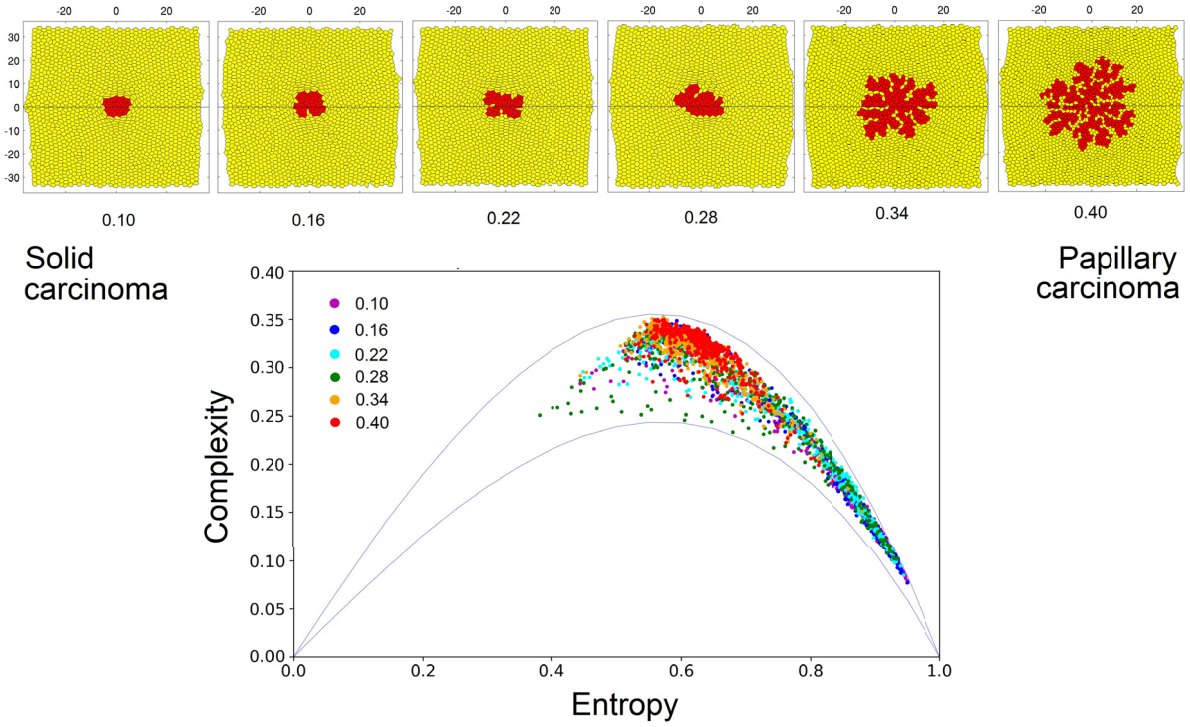

FIGURE 9. (*Top*) Examples of simulated carcinoma patterns at different values of intercalation parameter l_0 of normal cells. The intercalation parameter of cancer cells is fixed to $l_0^{\text{can}} = 0.1$. All patterns are obtained after intergration at the same time $t = 150$; (*bottom*) Complexity-entropy spectra taken from local values and shown on the H–C plane for carcinoma patterns at $l_0 = 0.1, 0.16, 0.22, 0.28, 0.34, 0.4$. Thin gray line encircles the admissible complexity C range for each H value.

Figure 9 shows the evolution of the tumor when changing the intercalation parameter l_0 from 0.1 to 0.4 and a fixed value $l_0^{\text{can}} = 0.1$. All structures are shown after integrating equations (2.1)–(2.7) from 0 to 150. We identify the structure, which is shown in the very first frame (Fig. 9, upper row, $l_0 = 0.1$), as a solid tumor. In this case, cancer and healthy cells have the same mobility, so the boundary between the media remains stable throughout the entire time of tumor development. The structure shown in the last frame of the figure is a papillary tumor (Fig. 9, upper row, $l_0 = 0.4$). In this case, the mobility of cancer tissue is much less than that of normal epithelium. It leads to the development of finger-like instability of the interface. One can notice that the instability occurs at values $l_0 > 0.28$. Comparing the first and last frames in the row, one can also notice that the tumor in the latter case develops much more intensively. Due to instability, the perimeter of the tumor increases many times over, a large number of F-cells appear, they are rapidly dividing. The complexity spectra of cancer structures reflect these processes. Figure 9(bottom) shows the local complexity spectra on a H–C plane. With a gradual increase in the intercalation parameter, one can see that the spectra shift to a region with a higher complexity value and lower entropy.

The following Figure 10 shows a similar evolution from a solid to a cribriform tumor with a gradual change in parameter l_0^{can} and a fixed value of parameter $l_0 = 0.1$. In this case, the mobility of cancer cells is higher, which is a more realistic situation since *in vivo* cancer cells, as a rule, belong to mesenchymal phenotype. The instability of the interface between the clusters of normal and cancer cells occurs at about $l_0^{\text{can}} \approx 0.22$. Figure 10(bottom) shows the local spectra of complexity on the H–C plane. We see that the cribriform structure in the last frame

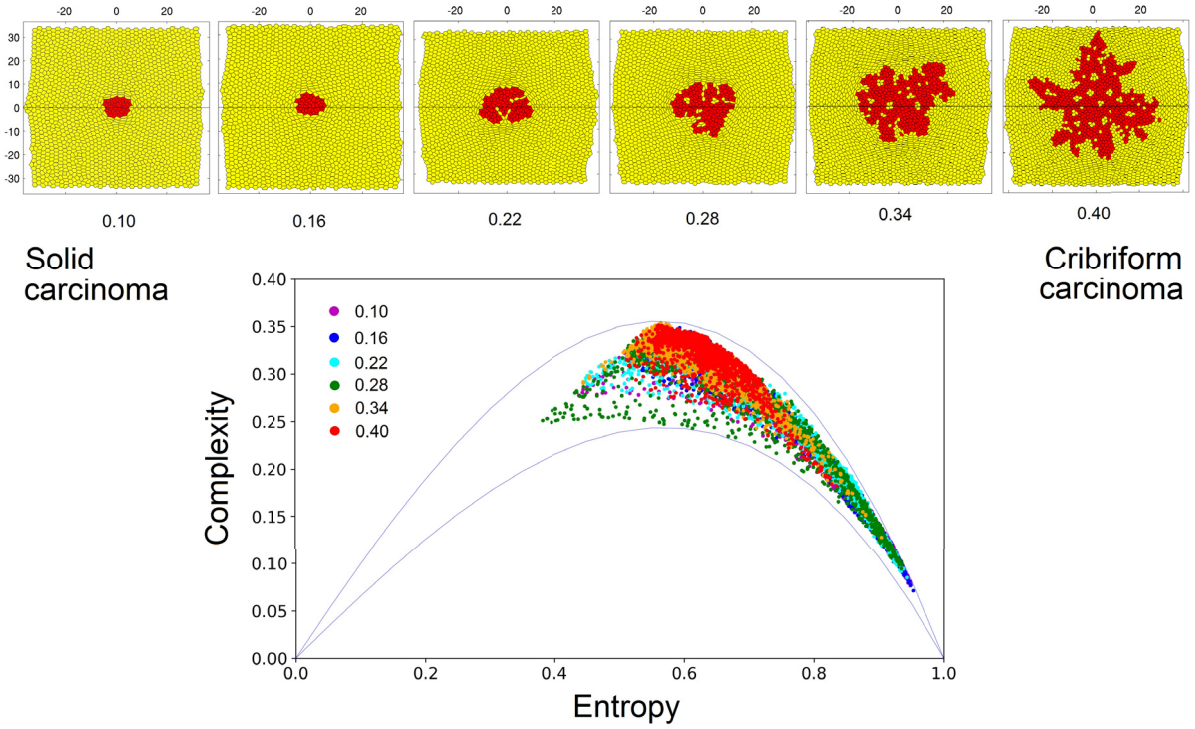

FIGURE 10. (*Top*) Examples of simulated carcinoma patterns at different values of intercalation parameter l_0^{can} of cancer cells. The intercalation parameter of normal cells is fixed to $l_0^{\text{can}} = 0.1$. All patterns are obtained after intergration at the same time $t = 150$; (*bottom*) Complexity-entropy spectra taken from local values and shown on the H–C plane for carcinoma patterns at $l_0^{\text{can}} = 0.1, 0.16, 0.22, 0.28, 0.34, 0.4$. Thin gray line encircles the admissible complexity C range for each H value.

(Fig. 10, upper row, $l_0^{\text{can}} = 0.4$) has the highest value of the complexity index. The final structure of the tumor includes small isolated islets of healthy cells, which are approximately equidistant from each other. It allows the tumor to grow much more intensively since there are many cells of the epithelial phenotype.

It is interesting to compare the structure at $l_0^{\text{can}} = 0.28$ with the final pattern at $l_0^{\text{can}} = 0.4$, which we identify as a cribriform tumor. The local spectrum of the first structure indicated in Figure 10(bottom) by green circles is mostly scattered over the H–C plane, demonstrating noise in healthy epithelial tissue due to the effect of tightness on the part of the tumor. The developed cribriform tumor in the last frame further enhances the entropy production since the deformations in the surrounding tissue become larger. However, a growing tumor simultaneously generates order redistributing cancer and healthy cells within an elastic pattern. The effect of increasing complexity from this order exceeds the entropy production that accompanies this process. We must admit that this example is an excellent illustration of the well-known S-theorem ("S" stands for self-organization) by Klimantovich [27]. As is known, any self-organizing structure also generates entropy into the surrounding space (dissipative structure in Prigogine's terminology [40]). The theorem formulated by Klimontovich asserts that the effect of self-organization on the entropy decrease is always stronger than the entropy generation in the surrounding thermostat.

To classify the architectural forms of tumors, we can apply the k-nearest neighbors (k-NN) algorithm, which is a simple and easy-to-implement supervised machine learning method. Figure 11 shows a map of various tumors developed at different ratios of intercalation parameters of normal and cancer cells. To compare tumors,

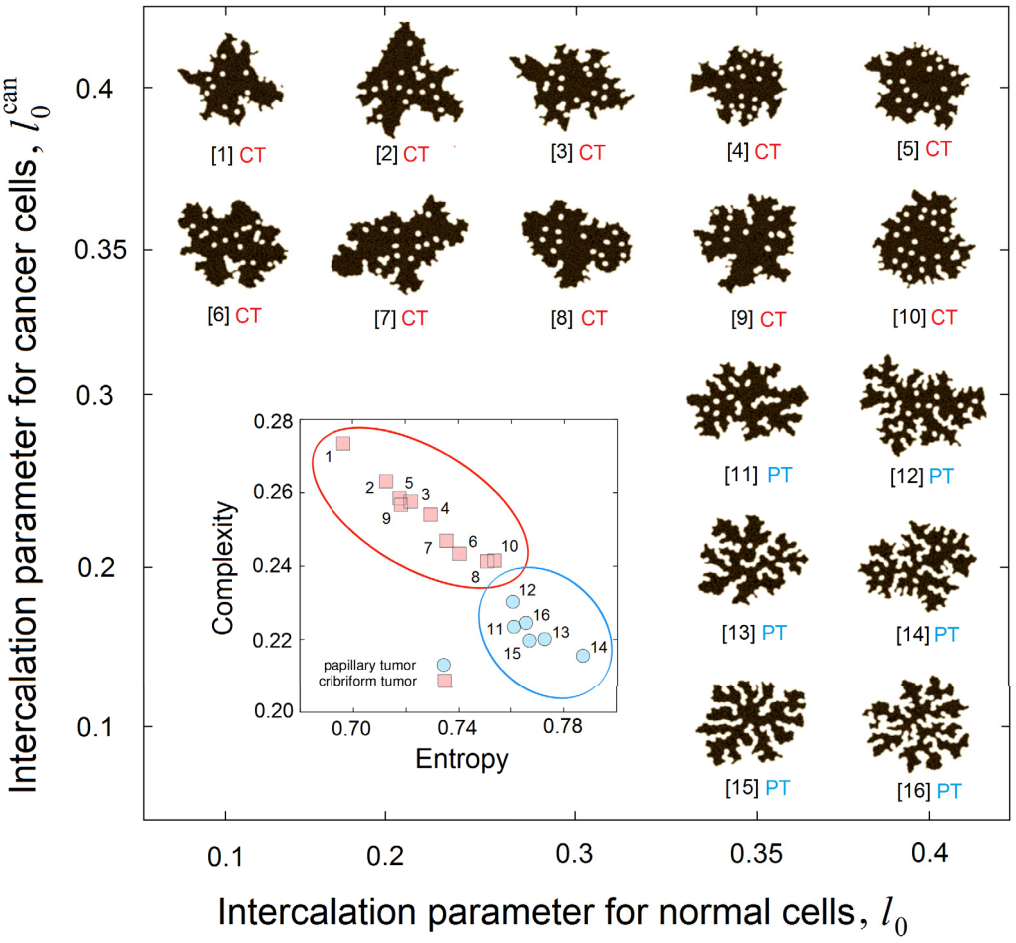

FIGURE 11. The map of architectural forms of invasive carcinoma developed at different values of the intercalation parameters l_0 and l_0^{can} for normal and cancer cells, respectively. All tumors formed over different periods of time, but consist of the same number of cells. Inset shows the results of tumores classification based on the k-nearest neighbors algorithm. On the H–C plane, the set of architectural forms surely falls into two distinct classes, cribriform (red squares) and papillary (blue circles) structures, for $k = 2$ and 3. The numbers of structures on the map match the numbers of the corresponding points shown on the H–C plane. The abbreviations CT and PT stand for the cribriform and papillary tumors, respectively.

we require that they fulfill the condition of the same volume. Thus, all the tumors shown in the figure consist of the same number of cells (300 cells). Since the elastic conditions for the development of carcinoma are different in all cases, the characteristic times of tumor formation in each case can significantly differ. We numbered all the tumors and calculated the entropy and complexity indices for each of them. The inset of Figure 11 shows this data on the H–C plane. The serial numbers of the points coincide with the numbers of the structures shown on the map.

As is known, in k-NN classification, each object is classified by a plurality vote of its neighbors, with the object being assigned to the class most common among its k nearest neighbors, where k is a positive integer, typically not so large. One can see from the inset (Fig. 11) that the initial set of tumors uniquely splits into

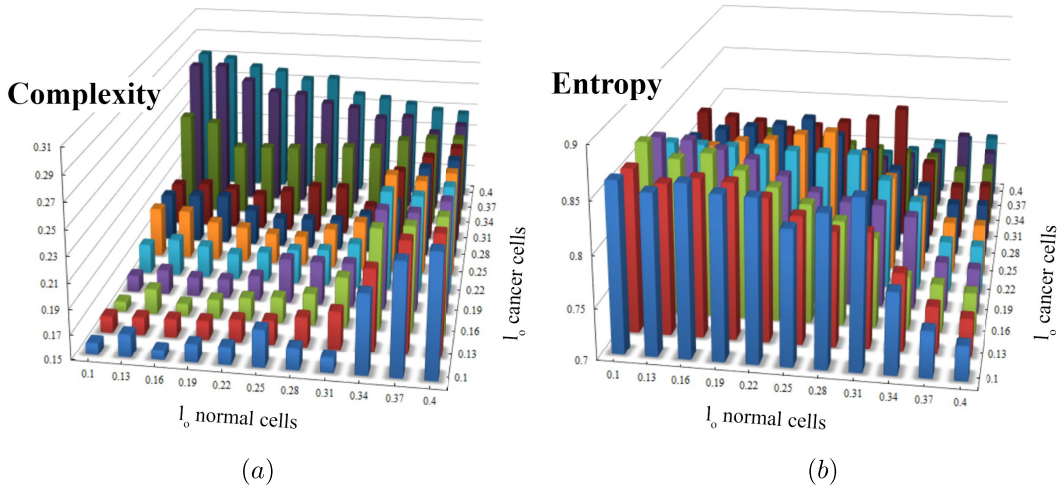

FIGURE 12. Variation of the global complexity estimate (a) and the spectral entropy (b) of carcinoma structures with the intercalation parameters l_0 and l_0^{can}. All patterns are obtained after intergration at the same time $t = 150$.

two classes both for $k = 2$ and for $k = 3$. The machine-based classification seems to correlate well with intuitive classification, which can be performed by direct visual inspection of the architectural forms of tumors. We identify these two classes with cribriform and papillary tumors. For example, we can look at tumors 9 and 10, which are transitional forms between the two classes. Although each of these tumors has characteristic features of both cribriform (inclusion of islands of normal cells) and papillary (finger-like outgrowths) structures, the k-NN algorithm classifies them as cribriform tumors.

Finally, Figure 12 summarizes the data for global complexity (a) and entropy (b) measures estimated for a variety of patterns generated at different values of the intercalation parameters.

6. Discussion and conclusions

In this work, we have used the measures of complexity and entropy to analyze two-dimensional images of cancer structures obtained in the numerical modeling of the development of carcinoma. To simulate an epithelium, we applied a previously developed individual-based model of the mechanical evolution of elastic epithelium. To generate tumor structures *in silico*, we used a mathematical model of heterogeneous carcinoma, which consists of the community of cancer cells performing various functions in the tumor. We demonstrated that classification of the tumor type based on a subjective perception of its spatial structure could be supported by quantitative characteristics. The emerging carcinomas differ significantly in terms of the complexity and entropy measures. It enables us to use these characteristics as tools for the objective classification of tumors.

To question whether we can use this technique to analyze the complexity of histological sections is still open. At present, the doctor makes his verdict after examining the histological section and relying on previous experience. This approach to determining the type of tumor should be recognized as subjective. The results obtained in this work imply that the complexity measurement could potentially be applied for the objective classification of tumors. However, we should recognize that the data obtained *in silico* create comfortable conditions for analysis. In the case of applying the technique to cancerous structures presented by histological sections, one needs first to solve several practical problems. It includes preliminary preparation of the image, works with the color palette of the picture, choosing the characteristic scale of the sample under study, and finally gaining experience in interpreting the data obtained.

Acknowledgements. This research was carried out with the financial support of the Ministry of Science and Higher Education of the Russian Federation in the framework of the program of activities of the Perm Scientific and Educational Center "Rational Subsoil Use". We are grateful to Dr. Brazhe for sharing his open-source Python-based software for calculating the complexity of textures. We are grateful to the referee for the idea to apply the k-nearest neighbors algorithm.

References

[1] C. Bandt and B. Pompe, Permutation entropy: a natural complexity measure for time series. *Phys. Rev. Lett.* **88** (2002) 174102.
[2] D.A. Bratsun, D.V. Merkuriev, A.P. Zakharov and L.M. Pismen, Multiscale modeling of tumor growth induced by circadian rhythm disruption in epithelial tissue. *J. Biol. Phys.* **42** (2016) 107–132.
[3] D.A. Bratsun, I.V. Krasnyakov and L.M. Pismen, Biomechanical modeling of invasive breast carcinoma under a dynamic change in cell phenotype: collective migration of large groups of cells. *Biomech. Model. Mechanobiol.* **19** (2020) 723–743.
[4] A. Brazhe, Shearlet-based measures of entropy and complexity for two-dimensional patterns. *Phys. Rev. E.* **97** (2018) 061301.
[5] P. Brodatz, Textures: A Photographic Album for Artists and Designers. Dover Publications, New York (1966).
[6] D. Chavey, Tilings by regular polygons – II: A catalog of tilings. *Comput. Math. Appl.* **17** (1989) 147–165.
[7] C.A. Chung, T.H. Lin, S.D. Chen and H.I. Huang, Hybrid cellular automaton modeling of nutrient modulated cell growth in tissue engineering constructs. *J. Theor. Biol.* **262** (2010) 267–278.
[8] V. Cristini and J. Lowengrub, Multiscale Modeling of Cancer: an Integrated Experimental and Mathematical Modeling Approach. Cambridge University Press, Cambridge (2010).
[9] J.P. Crutchfield, Between order and chaos. *Nat. Phys.* **8** (2012) 17–24.
[10] T.S. Deisboeck and G.S. Stamatakos, Multiscale Cancer Modeling. Chapman & Hall/CRC, Boca Raton (2011)
[11] E.V. Denisov, N.V. Litviakov, M.V. Zavyalova, V.M. Perelmuter, S.V. Vtorushin, M.M. Tsyganov, T.S. Gerashchenko, E. Yu. Garbukov, E.M. Slonimskaya and N.V. Cherdyntseva, Intratumoral morphological heterogeneity of breast cancer: neoadjuvant chemotherapy efficiency and multidrug resistance gene expression. *Sci. Rep.* **4** (2014) 4709.
[12] E. Denisov, T. Geraschenko, M. Zavyalova, N. Litviakov, M. Tsyganov, E. Kaigorodova, E. Slonimskaya, J. Kzhyshkowska, N. Cherdyntseva, V. Perelmuter, Invasive and drug resistant expression profile of different morphological structures of breast tumors. *Neoplasma* **62** (2015) 405–411.
[13] D.L. Dexter, H.M. Kowalski, B.A. Blazar, Z. Fligiel, R. Vogel and G.H. Heppner, Heterogeneity of tumor cells from a single mouse mammary tumor. *Cancer Res.* **38** (1978) 3174–3181.
[14] D. Drasdo and M. Loeffler, Individual-based models to growth and folding in one-layered tissues: Intestinal crypts and early development. *Nonlinear Anal.* **47** (2001) 245–256.
[15] M. Egeblad, E.S. Nakasone and Z. Werb, Tumors as organs: complex tissues that interface with the entire organism. *Dev. Cell* **18** (2010) 884–901.
[16] R. Farhadifar, J.C. Röper, B. Aigouy, S. Eaton and F. Jülicher, The influence of cell mechanics, cell–cell interactions, and proliferation on epithelial packing. *Curr. Biol.* **17** (2007) 2095–2104.
[17] P. Friedl, J. Locker, E. Sahai and J.E. Segall, Classifying collective cancer cell invasion. *Nat. Cell Biol.* **14** (2012) 777–783.
[18] T.S. Gerashchenko, M.V. Zavyalova, E.V. Denisov, N.V. Krakhmal, D.N. Pautova, N.V. Litviakov, S.V. Vtorushin, N.V. Cherdyntseva and V.M. Perelmuter, Intratumoral morphological heterogeneity of breast cancer as an indicator of the metastatic potential and tumor chemosensitivity. *Acta Nat.* **9** (2017) 56–67.
[19] C. Guillot and T. Lecuit, Mechanics of epithelial tissue homeostasis and morphogenesis. *Science* **340** (2013) 1185–1189.
[20] K. Guo, D. Labate and W.-Q. Lim, Edge analysis and identification using the continuous shearlet transform. *Appl. Comput. Harmon. Anal.* **27** (2009) 24–46.
[21] S. Häuser and G. Steidl, Convex multiclass segmentation with shearlet regularization. *Int. J. Comput. Math.* **90** (2013) 62–81.
[22] S. Häuser and G. Steidl, Fast finite shearlet transform: a tutorial. Available: http://arxiv.org/abs/1202.1773 (2014)
[23] L. He, L.R. Long, S. Antani and G.R. Thoma, Histology image analysis for carcinoma detection and grading. *Comput. Methods Progr. Biomed.* **107** (2012) 538–556.
[24] G.H. Heppner, Tumor heterogeneity. *Cancer Res.* **44** (1984) 2259–2265.
[25] H. Honda, T. Nagai and M. Tanemura, Two different mechanisms of planar cell intercalation leading to tissue elongation. *Dev. Dyn.* **237** (2008) 1826–1836.
[26] L.J. Kleinsmith, Principles of cancer biology. Pearson Benjamin Cummings (2006).
[27] Y.L. Klimontovich, Decrease in entropy in the process of self-organization. S-theorem. *Sov. Tech. Phys. Lett.* **9** (1983) 606–610.
[28] N.V. Krakhmal, M.V. Zavyalova, E.V. Denisov, S.V. Vtorushin and V.M. Perelmuter, Cancer invasion: patterns and mechanisms. *Acta Nat.* **7** (2015) 17–28.
[29] I.V. Krasnyakov, D.A. Bratsun and L.M. Pismen, Mathematical modelling of epithelial tissue growth. *Russ. J. Biomech.* **24** (2020) 375–388.
[30] G. Kutyniok and D. Labate, Shearlets. Multiscale analysis for multivariate data. Birkhäuser Boston, Boston (2012).
[31] S. Lamouille, J. Xu and R. Derynck, Molecular mechanisms of epithelial-mesenchymal transition. *Nat. Rev. Mol. Cell Biol.* **15** (2014) 178–196.
[32] J. Lober, F. Ziebert and I.S. Aranson, Collisions of deformable cells lead to collective migration. *Sci. Rep.* (2015) 9172.

[33] R. Lopez-Ruiz, Y.L. Mancini and X. Calbet, A statistical measure of complexity. *Phys. Lett. A.* **209** (1995) 321–326.
[34] J. Makki, Diversity of breast carcinoma: histological subtypes and clinical relevance. *Clin. Med. Insights Pathol.* **8** (2015) 23–31.
[35] L.M. Merlo, J.W. Pepper, B.J. Reid and C.C. Maley, Cancer as an evolutionary and ecological process. *Nat. Rev. Cancer* **6** (2006) 924–935.
[36] B.E. Miller, F.R. Miller and G.H. Heppner, Interactions between tumor subpopulations affecting their sensitivity to the antineoplastic agents cyclophosphamide and methotrexate. *Cancer Res.* **41** (1981) 4378–4381.
[37] I. Mizeva, V. Dremin, E. Potapova, E. Zherebtsov, I. Kozlov and A. Dunaev, Wavelet analysis of the temporal dynamics of the laser speckle contrast in human skin. *IEEE Trans. Biomed. Eng.* **67** (2020) 1882–2889.
[38] R. Polikar, A. Topalis, D. Green, J. Kounios and C.M. Clark, Comparative multiresolution wavelet analysis of ERP spectral bands using an ensemble of classifiers approach for early diagnosis of Alzheimer's disease. *Comput. Biol. Med.* **37** (2007) 542–558.
[39] G.E. Powell and I.C. Percival, A spectral entropy method for distinguishing regular and irregular motion of Hamiltonian systems. *J. Phys. A: Math. Gen.* **12** (1979) 2053–2071.
[40] I. Prigogine and G. Nicolis, Self-Organization in Non-Equilibrium Systems. Wiley (1977).
[41] H.V. Ribeiro, L. Zunino, E.K. Lenzi, P.A. Santoro and R.S. Mendes, Complexity-entropy causality plane as a complexity measure for two-dimensional patterns. *PLoS ONE* **7** (2012) e40689.
[42] O.A. Rosso, H.A. Larrondo, M.T. Martin, A. Plastino and M.A. Fuentes, Distinguishing Noise from Chaos. *Phys. Rev. Lett.* **99** (2007) 154102.
[43] I. Ruben, R.-R. Reinaldo, V.-R. Fernando *et al.*, Tumor growth modelling by cellular automata. *Math. Mech. Complex Syst.* **5** (2017) 239–259.
[44] M. Salm and L.M. Pismen, Chemical and mechanical signaling in epithelial spreading. *Phys. Biol.* **9** (2012) 026009.
[45] C.E. Shannon, A mathematical theory of communication. *Bell Syst. Tech. J.* **27** (1948) 379–423.
[46] H.P. Sinn and H. Kreipe, A brief overview of the WHO classification of breast tumors, 4th edition, focusing on issues and updates from the 3rd edition. *Breast Care* **8** (2013) 149–154.
[47] K-Y. Su and W-L. Lee, Fourier transform infrared spectroscopy as a cancer screening and diagnostic tool: a review and prospects. *Cancers* **12** (2020) 115.
[48] D. Tabassum and K. Polyak, Tumorigenesis: it takes a village. *Nat. Rev. Cancer* **8** (2015) 473–483.
[49] I. Viktorinova, L. Pismen, B. Aigouy and C. Dahmann, Modeling planar polarity of epithelia: the role of signal relay in collective cell polarization. *J.R. Soc. Interface.* **8** (2011) 1059–1063.
[50] M. Zanin, L. Zunino, O.A. Rosso and D. Papo, Permutation entropy and its main biomedical and econophysics applications: a review. *Entropy* **14** (2012) 1553–1577.
[51] L. Zunino and H.V. Ribeiro, Discriminating image textures with the multiscale two-dimensional complexity-entropy causality plane. *Chaos Solitons Fract.* **91** (2016) 679–688.